RESEARCH ARTICLE | FEBRUARY 13 2023

Programmable vapor-phase metal-assisted chemical etching for versatile high-aspect ratio silicon nanomanufacturing **9**

Lukas L. Janavicius 💿 ; Julian A. Michaels 💿 ; Clarence Chan 💿 ; Dane J. Sievers 💿 ; Xiuling Li 🗷 💿



Appl. Phys. Rev. 10, 011409 (2023) https://doi.org/10.1063/5.0132116







Applied Physics Reviews

Special Topic: Frontiers in energy materials research: novel measurement, modeling and processing approaches

Submit Today





Programmable vapor-phase metal-assisted chemical etching for versatile high-aspect ratio silicon nanomanufacturing o

Cite as: Appl. Phys. Rev. 10, 011409 (2023); doi: 10.1063/5.0132116 Submitted: 26 October 2022 · Accepted: 17 January 2023 · Published Online: 13 February 2023 · Publisher error corrected: 16 February 2023

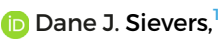








Lukas L. Janavicius, 🗀 Julian A. Michaels, 🕞 Clarence Chan, 🕞 Dane J. Sievers, 🕞 and Xiuling Li^{1,2,a} 🕞











- Department of Electrical and Computer Engineering, Holonyak Micro and Nanotechnology Laboratory, University of Illinois at Urbana-Champaign, Urbana, Illinois 61801, USA
- 2 Department of Electrical and Computer Engineering, Microelectronics Research Center, The University of Texas, Austin, Texas 78758, USA

ABSTRACT

Defying the isotropic nature of traditional chemical etch, metal-assisted chemical etching (MacEtch) has allowed spatially defined anisotropic etching by using patterned metal catalyst films to locally enhance the etch rate of various semiconductors. Significant progress has been made on achieving unprecedented aspect ratio nanostructures using this facile approach, mostly in solution. However, the path to manufacturing scalability remains challenging because of the difficulties in controlling etch morphology (e.g., porosity and aggregation) and etch rate uniformity over a large area. Here, we report the first programmable vapor-phase MacEtch (VP-MacEtch) approach, with independent control of the etchant flow rates, injection and pulse time, and chamber pressure. In addition, another degree of freedom, light irradiation is integrated to allow photo-enhanced VP-MacEtch. Various silicon nanostructures are demonstrated with each of these parameters systematically varied synchronously or asynchronously, positioning MacEtch as a manufacturing technique for versatile arrays of threedimensional silicon nanostructures. This work represents a critical step or a major milestone in the development of silicon MacEtch technology and also establishes the foundation for VP-MacEtch of compound semiconductors and related heterojunctions, for lasting impact on damage-free 3D electronic, photonic, quantum, and biomedical devices.

© 2023 Author(s). All article content, except where otherwise noted, is licensed under a Creative Commons Attribution (CC BY) license (http:// creativecommons.org/licenses/by/4.0/). https://doi.org/10.1063/5.0132116

I. INTRODUCTION

Nanostructures have provided new kinds of possibilities in the miniaturization and performance enhancement of modern electronic and optoelectronic devices. However, many challenges remain before scalability is fully achieved. 1-3 Along with lithography and deposition, etching plays a significant role in semiconductor fabrication processes. Highly directional etching using reactive ion etch (RIE) has enabled the aggressive scaling of transistors from planar channel to high-aspect ratio finFETs, through silicon (Si) vias (TSVs), novel photonic structures, and biological cell-nanomaterial interactions. 4-6 However, the achievable aspect ratio and sidewall verticality using RIE are limited, and more importantly, the high-energy ion-induced damage cannot be repaired readily without significant thermal budget or material loss. Metal-assisted chemical etching (MacEtch or MACE), on the other hand, is a uniquely anisotropic chemical etching method, that defies the isotropic nature of conventional wet etch through local catalysis and charge transfer effect. MacEtch enabled site-controlled semiconductor nanostructure fabrication^{8–11} with an unmatched aspect ratio (as high as $10\,000:1)^{12}$ and an etch rate as high as $>3\,\mu\mathrm{m}~\mathrm{min}^{-1}$ (Ref. 13) at or near room temperature. MacEtch was first reported as a method to generate porous Si using a discontinuous layer of catalyst metal film under an open circuit in 2000.¹⁴ Site-specific vertical etching was subsequently achieved by patterning the metal catalyst film using self-assembled dendritic Ag network from AgNO₃ solution or various lithographic methods. ¹⁵ This technology continues to advance through the investigation of the fundamental mechanism, process parameters, properties, and CMOS compatibility, 16 extending its applicability to many semiconductors, including Ge, ¹⁷ GaAs, ^{18–21} InP, 22,23 GaN, 24,25 SiC, 26,27 β -Ga₂O₃, $^{28-30}$ and related device applications.

a) Author to whom correspondence should be addressed: xiuling.li@utexas.edu

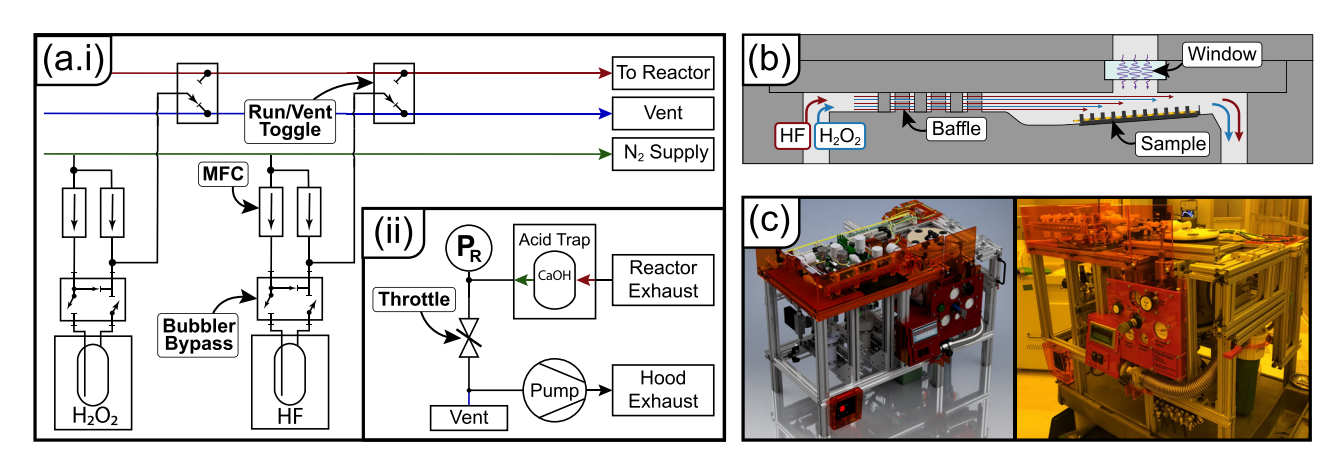


FIG. 1. Vapor-phase MacEtch (VP-MacEtch) reactor design and image of the completed system. (a-i) Upstream gas circuit diagram, parallel mass flow controllers (MFCs) independently control vapor delivery of HF and H_2O_2 . The labeled valves play an important role in pulse-mode VP-MacEtch; the run/vent toggle prevents the reactant from entering the chamber and vents the line, while the bypass closes off the bubbler and bypasses the line with N_2 . (a-ii) Downstream gas circuit, the reactor pressure throttle control and measurement (P_R) are located after the CaOH acid trap. (b) Cross section view of the VP-MacEtch reactor, the baffle distributes the flow across the sample, the sample pocket accommodates up to a 2-in. silicon wafer tilted at 5° to reduce the effects of reactant consumption across the sample, and the magnesium fluoride (MgF₂) window transmits 172 nm VUV light in a 1-in. diameter over the sample's center. (c) Render and photograph of VP-MacEtch reactor system.

Fundamentally, MacEtch is an open circuit local redox reaction consisting of an acid (or base) etchant and oxidant. In the case of Si, the pair is HF/H_2O_2 for which the cathodic and anodic reactions are shown in Eqs. (1) and (2), respectively. Combining the two components yields the overall reaction in Eq. (3),

$$\label{eq:H2O2} H_2O_2 + 4H^+ + 2e^-_{(Si)} \xrightarrow{catalyst} 2H_2O + 2h^+_{(Si)} + H_{2(g)}, \qquad (1)$$

$$Si_{(s)} + 6HF + 4h_{(Si)}^{+} \rightarrow H_{2}SiF_{6} + 4H^{+}, \tag{2}$$

$$Si + H_2O_2 + 6HF \xrightarrow{catalyst} 2H_2O + H_2SiF_6 + H_{2(g)}. \tag{3} \label{eq:sigma}$$

On contact with the catalyst, the oxidant is reduced by extracting electrons (or equivalently injecting holes) from the Si. The presence of these electronic holes changes the oxidation state of the silicon local to the catalyst and enables the oxidation and subsequent removal of Si. As the Si is removed beneath the catalyst, it sinks and contacts unreacted material, continuing the reaction to form a negative image of the catalytic mask. The reduction of the oxidant, Eq. (1), may occur without the presence of HF. If the rate of charge transfer from the oxidant's reduction exceeds the rate of material removal by the etchant, controlled by mass transport, excess holes diffuse away from the catalyst causing undesirable porosity and a certain degree of isotropic etching in the resulting features. ^{13,31} The molar ratio of H_2O_2 to HF is defined in Eq. (4), and in the liquid-phase, low $\rho[H_2O_2]$ is typically required to produce non-porous, vertical sidewalls, ¹³

$$\rho[H_2O_2] = \frac{H_2O_2[M]}{HF[M] + H_2O_2[M]}.$$
 (4)

Regardless of the catalyst material, the gaseous products in Eq. (3), mainly H_2 , bubble up on the catalyst layer which could cause etch non-uniformity or total delamination of the catalyst in conventional liquid MacEtch. 31,32 The impact of metal catalyst shift or delamination may be mitigated with one of the following approaches: the self-

anchored (SAC) MacEtch, which uses of a thin, nanoporous catalyst to permit the passage of the bubbles and etchants, helping adhesion to the substrate; lowering $\rho[H_2O_2]$ to limit H_2 gas production; or adding surfactants to the etching solution which lowers the surface tension and decreases the size of the bubbles. 31,33,34 However, none of these methods can eliminate the effects caused by the gaseous products in a liquid solution and they all impose additional processing constraints. For example, the nanoscale pores in SAC-MacEtch enhance mass transport of reactants, but the nanowires formed by the pores act as light scattering sites (e.g., in the case of black Si), making the process less suitable for reflective optics and MEMS applications. Likewise, controlling delamination by limiting $\rho[H_2O_2]$ improves etch stability, but greatly reduces the etch rate. ^{13,37} Finally, the addition of surfactants is widely used to enhance mass transport and reduce the effect of capillary-induced nanowire agglomeration, but is not effective at preventing delamination and makes the process incompatible with polymer layers used in some 3D-MacEtch processes.

In contrast, MacEtch taking place in the vapor phase (VP) ensures an identical phase of reactants and products, eliminating the possibility of delamination. Hildreth and Schmidt reported the first demonstration of VP-MacEtch by suspending a silicon sample upside down away from the heating source, with randomly dispersed Au nanoparticles, over a heated solution of HF/H₂O₂.³⁴ Following this study, Kim et al. demonstrated VP-MacEtch of Si with a titanium nitride catalyst by thermally vaporizing the HF/H₂O₂ solution in proximity to the heated surface-side-up sample, eliminating condensation.¹⁶ However, both studies reported porous surface formation at low aspect ratios and etch rates less than $0.25 \,\mu\mathrm{m} \,\mathrm{min}^{-1}$. Recently, Romano et al. reported porosity-free, high-aspect ratio VP-MacEtch by forming Si nanowires (10–100 nm in diameter) 107 μ m tall with a self-anchored platinum-silicide (Pt-Si) catalyst. 12 Notably, Romano et al. reported failure to pattern transfer Pt-metal with the same process, instead relying on SAC-MacEtch with the nanoporous Pt-Si

catalyst. ¹² In agreement with Hildreth and Schmidt, Romano *et al.* found that the presence of H_2O_2 in the vaporized solution serves to increase porosity with little impact on the etch rate compared to ambient oxygen, and therefore may be omitted from the solution. ^{12,34}

The major limitation preventing thermal-vapor MacEtch from replicating the success of conventional liquid-phase results, e.g., etch rates exceeding 3 μ m min⁻¹, is the lack of independent control of the acid etchant and oxidant. When ambient oxygen is used as the oxidizing component of the VP-MacEtch reaction, $\rho[\mathrm{H}_2\mathrm{O}_2]$ may only be controlled by diluting HF. Romano *et al.* reported an increase in the etch rate (up to $0.4\,\mu$ m min⁻¹) using an unpatterned self-anchored-catalyst by increasing the concentration of HF in the vaporized solution. However, pattern transfer was unstable at higher etch rates, so the etch was slowed (below $0.1\,\mu$ m min⁻¹) by diluting the HF. Because the vapor flows horizontally across the sample's surface, the fixed oxidant supply is rapidly depleted as [HF] increases causing non-uniform etching.

To address the limitations of independent control of all reactants in the vapor phase, for the first time, we present a fully computer-controlled programmable VP-MacEtch system (Fig. 1) that operates under vacuum. By independently switching HF and $\rm H_2O_2$ with the desired flow rates, injection and pulse time, chamber total and partial pressures, and sample temperature, we demonstrate a versatile array of high-aspect and controlled curvilinear Si nanostructures over large areas. In addition, a light source is integrated to allow photo-enhanced VP-MacEtch ($h\nu$ -MacEtch) of Si, producing a basin-like etch profile around a CMOS-compatible Ruthenium catalyst.

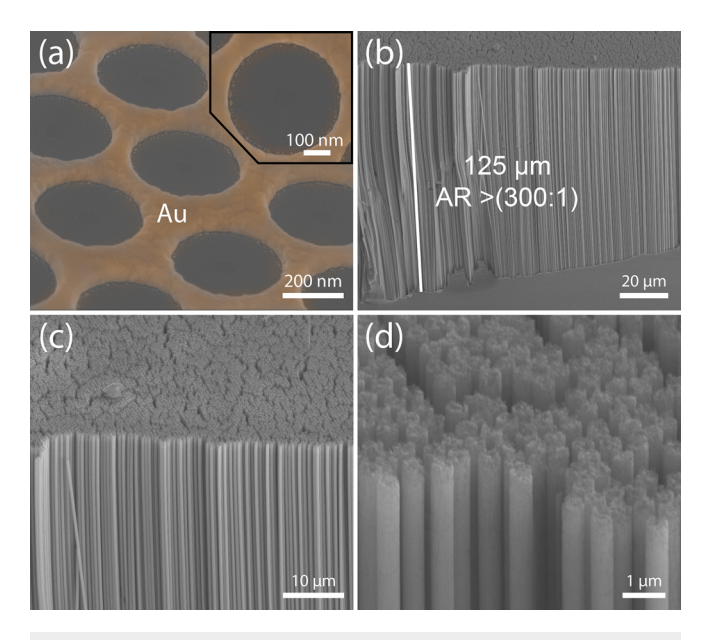


FIG. 2. Agglomeration-free, high-aspect ratio vertical nanowire array. (a) Gold catalyst mesh pattern on Si(100); 60 nm metal thickness, 400 nm hole diameter, and 100 nm hole spacing. (b) 50° tilted SEM images of an array of 400 nm diameter, 125 μ m tall (AR > 300) \langle 100 \rangle oriented nanowires, formed by etching for 12 h at f[HF] = 200 sccm, $f[H_2O_2] = 1200$ sccm, $\rho_v[H_2O_2] = 1.3$ Torr, $P_R = 600$ Torr, and $\rho[H_2O_2] = 0.2$. (c) and (d) high-magnification images of (b) showing the nanowire top segment and the tips. Note that the rough tip morphology is due to gold deposition under the spherical shadow mask (see the supplementary material Fig. S1).

II. RESULTS AND DISCUSSION

A. High-aspect ratio, high-density silicon nanowires without agglomeration

Figure 2 shows an array of Si nanowires of 400 nm diameter, 100 nm spacing, and 125 μ m tall (aspect ratio of 312:1), formed by VP-MacEtching for 12 h, where the carrier gas flow of HF and H₂O₂ is f[HF] = 200 sccm and $f[H_2O_2] = 1200$ sccm, respectively, the H_2O_2 vapor pressure is $p_v[H_2O_2] = 1.3$ Torr, the reactor working pressure is $P_R = 600$ Torr, and the H_2O_2 molar ratio is $\rho[H_2O_2] = 0.2$. The nanowires appear highly vertical with respect to the (100) direction. Remarkably, with the close spacing and high aspect ratio, the nanowires do not show any agglomeration. The dry nature of VP-MacEtch is particularly useful for high-aspect ratio features, enabling the etching of nanoscale patterns greater than $100 \, \mu m$ deep without collapsing or agglomeration. In contrast, despite drying in a heated solvent bath, agglomeration of the nanowires of similar height and density is apparent when etched in the liquid phase. 13 In agreement with both Hildreth and Schmidt³⁴ and Romano et al., ¹² the VP-MacEtch-nanowires in this report lacks the formation of mesoporous silicon at the etch front. It was proposed by Kong et al. that porous silicon formation with a gold catalyst results from the accumulation, diffusion, and redeposition of metal ions on the surface of the catalyst; ⁴¹ Chern et al. reported Ag catalyst dissolution leads to porous silicon sidewalls.⁴² Evidently, in the vapor phase, there is no medium to facilitate the transport of metal ions, hence the absence of porosity. In addition, porosity formation can be suppressed or eliminated by the much shorter residence time of the etchant precursors due to the constant flux in the chamber, which leaves no local accumulation of oxidant, supporting the absence of porosity observed. Additional experiments will be performed to confirm the underlying reason for the porosity absence. We note that the uneven spacing or gaps between nanowires can be attributed to nanosphere lithography nonuniformity—line defects in the otherwise closely packed nanospheres, and the porosity present on the nanowire tips are due to gold deposition under the spherical shadow mask (Fig. S1). Note that although it takes place in the vapor phase, VP-MacEtch is inherently damage-free to the semiconductor crystal, just like in the liquid phase, because of the same plasma-free nature.

The nominal etch rate of 137 nm/min achieved here with the $p_v[{\rm H_2O_2}]=1.3$ Torr peroxide source is substantially lower than some reported in the liquid phase, where etch rates for similar Au–Si pattern geometries may exceed this rate by an order of magnitude depending on doping level and etching chemistry. ^{13,43} Although MacEtch rate does increase with the doping level, the primary factor controlling the etch rate is the absolute flux of reactants delivered to the sample as demonstrated further below. Additionally, the depletion of sources over time and distance likely results in a non-linear etch rate with etching time, as analyzed in the supplementary material (Figs. S4 and S5).

B. Synchronous pulse-mode VP-MacEtch

To mitigate source delivery issues, pulsed-mode MacEtch, only possible with fully independently controlled vapor phase etchants, is developed. In this etch mode, the flow of HF and $\rm H_2O_2$ can each be turned on and off for a programmed period of time, synchronously or asynchronously. Figure 3 shows a highly uniform array of Si nanowires of 400 nm diameter, 100 nm spacing, and $16~\mu m$ tall (aspect ratio of 40:1), formed

by synchronously pulsing the reactants on and off with 5 min period, 50% duty cycle, and 30-min duration at f[HF]=800 sccm, $f[H_2O_2]=1200$ sccm, $p_v[H_2O_2]=2.1$ Torr and $\rho[H_2O_2]=0.091$ during the on-period, and with a total flow of $f[N_2]=2000$ sccm during the off-period to maintain the chamber pressure. Figure 3(a) is a low-magnification view of the array with insets indicating measurement locations of the bulk [Fig. 3(b), $L_{100}=16~\mu{\rm m}$] and the leading edge closest to the gas precursor injection inlet, [Fig. 3(c), $L_{edge}=17.4~\mu{\rm m}$]. Figure 3(d) is a view of the nanowire sidewall scalloping, shown in greater detail in Fig. 3(e), aligned to the period of pulses in the recipe (N_2 flow not shown).

Normalizing the etch rate by the total time reactants flown into the reactor (15 min) yields an etch rate at the leading edge of 1.16 μ m min⁻¹ For comparison, nanowires processed continuously for 15 min under identical conditions offer a marginally lower etch rate of 1.11 μ m min⁻¹ at the leading edge. Unlike continuous mode etching, each pulse in Fig. 3(d) creates a small scallop on the nanowire's

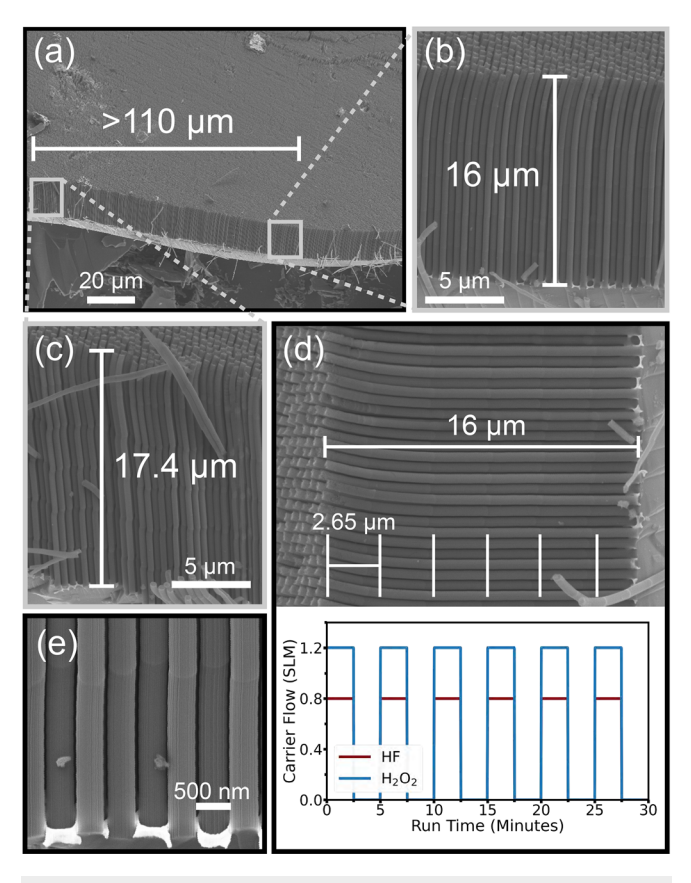


FIG. 3. Uniform nanowire array by synchronous pulse-mode VP-MacEtch. Reactants are pulsed with a 5 min period, 50% duty cycle, and 30-min duration under the following conditions; $\rho[H_2O_2]=0.091,\,P_R=600\,{\rm Torr},\,p_\nu[H_2O_2]=2.1\,{\rm Torr},$ and a constant volumetric flow of 2000 sccm. All cross-sectional SEM images are taken at 50° stage tilt. (a) Low magnification view of the highly uniform, bulk nanowire array. (b) Magnified view of nanowires approximately $100~\mu m$ away from the sample's leading edge. (c) Leading edge of the nanowire array, the diffusion of reactants is enhanced by the additional diffusion surface which increases the etch rate in this region. (d) Magnified view of (b) with the sidewall scallops caused by the pulse aligned to the recipe's period, and (e) high-magnification view of [(b) and (d)] sidewall scalloping and catalyst–substrate interface.

sidewall [Fig. 3(e)] with a mean spacing of 2.65 μ m. The scallop formation is likely an artifact of abruptly toggling the bubbler bypass valve [Fig. 1(a)]. The bubbler pressures are not independently regulated, so as the headspace reaches equilibrium during the off-cycle the internal pressure rises to cause a momentary spike in pressure between 5 and 10 Torr. Despite the minor sidewall perturbation, the ability to controllably and rapidly pause and resume etching may enable integration with other vapor-phase processes such as atomic layer deposition (ALD)/atomic layer etching (ALE).

C. Uniformity enhancement through synchronous pulsing

Multiple factors can affect the etch rate over distance and time. The horizontal flow arrangement of the VP-MacEtch reactor enables line-of-sight for external excitation sources (photo-enhanced MacEtch results to be presented later); however, as the reactants flow across the sample, they are consumed which leads to a lateral positional dependence across the wafer in etch rate. This effect manifests as an increased etch rate at the leading edge (closest to the gas precursor injection inlet). A similar edge-effect has been reported for the Au MacEtch of Si nanowires in the liquid phase, as there is a higher diffusion flux at the sample's border. The relative length difference between the leading-edge (L_{edge}) and nanowires $\gtrsim 100~\mu m$ away in the bulk (L_{100}) is quantified by $\Delta L_{100} = \frac{L_{edge} - L_{100}}{L_{edge}}$. For the high-aspect ratio nanowire array in Fig. 2, $L_{edge} = 125~\mu m$ (137 nm/min at the edge) and $L_{100} = 96~\mu m$ (105 nm/min in the bulk), so $\Delta L_{100} = 23.2\%$.

In contrast, the synchronously pulsed nanowire array in Fig. 3 with $\Delta L_{100} = 8.75\%$ shows dramatically improved uniformity. For comparison, nanowires processed continuously for 15 min under identical conditions offer a marginally lower etch rate of $1.11\,\mu\mathrm{m}$ min⁻¹ at the leading edge but a higher variation in the bulk $\Delta L_{100} = 13.1\%$ (Fig. S5). Although both continuous and pulsed etching offer improved uniformity compared to the high-aspect ratio array (Fig. 2, $\Delta L_{100} = 23.1\%$), it is certain that bypassing the sources before they experience depletion allows the vapor pressure in the bubbler's headspace to recover ensuring constant vapor delivery.⁴⁷

Both pulsed and continuously etched nanowires vastly outperform the results reported for thermal vapor MacEtch. The SAC-VP-MacEtch process demonstrated by Romano et al., 22 achieved a bulk depth of $L_{100} = 15 \mu m$ (120 nm/min) and a leading edge depth of $L_{edge} = 19.5 \,\mu\text{m}$ (165 nm/min) after 2 h with a uniformity of $\Delta L_{100} = 23.1\%$. Additionally, changing the substrate temperature from 55 °C to 40 °C dramatically reduced the uniformity to ΔL_{100} \geq 40%. Decreasing substrate temperature increases the amount of HF adsorbed onto the sample, which requires additional oxidant to maintain the balance of the reaction. Coupled with the dependence on reactant supply discussed above, this strongly suggests the depletion of atmospheric oxygen in thermal vapor MacEtch is the source of its non-uniformity. Note that the metric used to quantify uniformity in the work by Romano et al. was the edge-to-center variation, ΔL_{center} = 15.2% for the synchronously pulsed sample, which is not used in this work to account for variations in sample size. Although the deviation between the change in length of ΔL_{100} and ΔL_{center} is larger than that reported by Romano et al., the relative comparison between the results still holds over a larger area (details discussed in the supplementary material, Fig. S7). 12

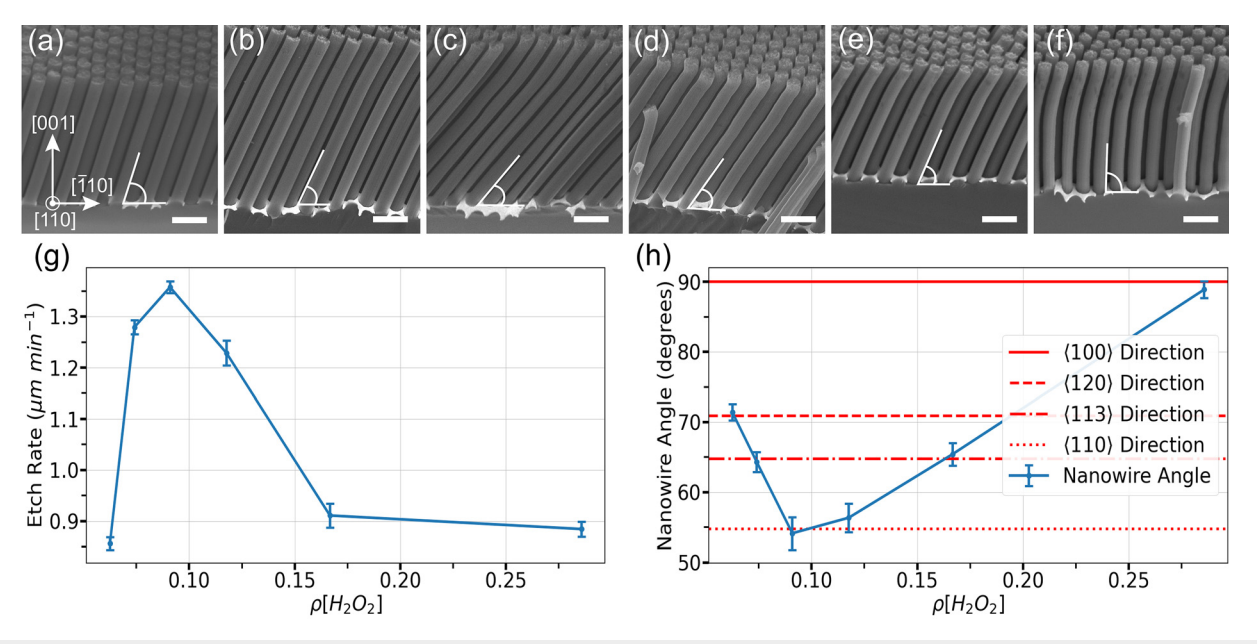


FIG. 4. Nanowire orientation control by vapor phase reactant concentration for higher tunability than liquid phase. [(a)–(f)] Cross-sectional 50° tilted SEM images of nanowires etched for 5 min at $p_V[H_2O_2] = 2.1$ Torr, $P_R = 600$ Torr, and $\rho[H_2O_2] \times 10^2 = 6.25$, 7.41, 9.09, 11.8, 16.7, 28.6, respectively (H₂O₂ flow was kept constant while HF was varied) on Si(100) substrates. All scale bars represent 1 μ m. (g) Plot of the corresponding etch rates vs H₂O₂ molar ratio. (h) Nanowire angle relative to Si(100) plane plotted against H₂O₂ molar ratio. Red lines indicate the angle of various crystal directions relative to the Si(100) plane (Fig. S8).

D. Asynchronous pulse-mode VP-MacEtch

1. Vapor phase chemistry-controlled nanowire crystal orientation

Another unique feature of MacEtch is its ability to anisotropically remove material without a line of sight from the top of the substrate to the bottom of the feature, in contrast to RIE. This property allows for tilted and curvilinear nanowire formation by changing the preferred etch orientation through control of the etching solution's composition, or temperature, manipulating the mass transport and carrier generation rates. ^{48–51} Additionally, the ability to rapidly change etching conditions in the vapor phase enables real-time control over the etching direction.

 $\langle 100 \rangle$ is generally the preferred etching direction of Au MacEtch of Si, because the (100) plane has the lowest number of Si-backbonds and therefore requires the least amount of backbond weakening (oxidation) and bond cleaving (material removal) to advance the etch forward. Therefore, by using different substrate orientations, such as Si(110) or Si(111), the resulting $\langle 100 \rangle$ nanowires form at an angle relative to the substrate surface normal. However, non-vertical nanowires may also be formed on Si(100) substrates by controlling the relative rate of silicon backbond oxidation [Eq. (2)] to the removal of the oxidized material [Eq. (1)]. Kim *et al.* demonstrated etching along the $\langle 110 \rangle$ direction for the HF/H₂O₂ system under two scenarios (details in the supplementary material). So Scenario 1: the absolute molar concentration (low dilution) of [HF] is high, and ρ [H₂O₂] is increased until alternate etch orientations are observed. Scenario 2: The absolute concentration of [H₂O₂] is high and ρ [H₂O₂] is decreased.

To understand how control over nanowire orientation extends to the vapor phase, nanowires were formed by MacEtching continuously at varying molar ratios ($p[H_2O_2]$). Figure 4 shows nanowire arrays etched continuously for 5 min at $p_v[H_2O_2] = 2.1$ Torr, $P_R = 600$ Torr, and

 $\rho[H_2O_2]\times 10^2=6.25, 7.41, 9.09, 11.8, 16.7, and 28.6 for Figs. 4(a)–4(f), respectively, achieved by varying <math display="inline">f[\mathrm{HF}]$ only (see Table I for flow rates). Figures 4(g) and 4(h) show the average etch rates (taken at $<20~\mu\mathrm{m}$ from the leading-edge) and the nanowire angle relative to the cleaved $\langle\bar{1}\,10\rangle$ direction, respectively, plotted against the molar ratio $\rho[\mathrm{H}_2\mathrm{O}_2]$. The overlaid lines in red in Fig. 4(h) represent the angle of published nanowire orientations achieved by MacEtch projected onto the Si(110) plane. 50,53

The etch rate and tilt-angle of the nanowires (Fig. 4) closely mirror the reported H_2O_2 molar ratio dependence in the liquid phase. ^{50,53} Referring to the processing conditions in Table I, because $f[H_2O_2]$ is held constant when $\rho[H_2O_2]$ is low, the total flow through the reactor is maximized. The additional carrier gas dilutes $[H_2O_2]$ placing the etch into *Scenario 1*, but despite low values of $\rho[H_2O_2]$ (relative to the liquid phase) non- $\langle 100 \rangle$ oriented nanowires are formed. ³¹ If f[HF] is increased further, the etch is expected to return to the $\langle 100 \rangle$ orientation; however, the HF source is unable to provide a constant vapor

TABLE I. Slanted nanowire process conditions, with a constant peroxide output of $f_{out}[H_2O_2] = 4.2$ sccm. Relative $[H_2O_2]$ is calculated relative to total molar flow through the reactor [Eq. (5) reported in Sec. III].

Case	f[HF] (sccm)	f[H ₂ O ₂] (sccm)	f _{out} [HF] (sccm)	Relative $[H_2O_2]$	$\rho[H_2O_2]\times 10^2$
a	1200	1200	63.2	0.18%	6.25
b	1000	1200	52.6	0.19%	7.41
c	800	1200	42.2	0.21%	9.09
d	600	1200	31.6	0.23%	11.8
e	400	1200	21.1	0.26%	16.7
f	200	1200	10.53	0.30%	28.6

output above 1200 sccm (Fig. S4). As f[HF] decreases, the relative rate of hole injection increases until the maximum etch rate of 1.36 μm min⁻¹ is reached. Although the average angle of 54.1° indicates a $\langle 110 \rangle$ orientation, alternate etch directions may also produce this angle (Fig. S8). The sample cleaving process before imaging introduces uncertainty in these measurements. For example, grooving on the cleaved surface is visible in Fig. 4(d), which indicates the reference direction may not be $\langle \bar{1}10 \rangle$; however, the measured nanowire tiltangles and their respective etch rates align well with reported orientation-dependent MacEtch, where stoichiometrically balanced orientations, such as (110), exceed the etch rate of the (100) direction. 46,51,53,54 Further decreasing f[HF] reduces the etch rate, indicating the reaction is limited by the removal of silicon as in Scenario 2. As expected, the decreased flow in the reactor maximizes [H2O2] and $\rho[H_2O_2]$, so the limited HF prefers the removal of the $\langle 100 \rangle$ orientation. Once again, unlike in the liquid phase, the excess hole generation does not lead to porosity on the nanowire's sidewall.

2. Kinked nanowires

Synchronous pulsing VP-MacEtch ensures that during the off-cycle, both reactants are consumed at similar rates and the process halts. However, if the H_2O_2 flow is kept constant while the HF flow is either shut off or reduced periodically, $\rho[H_2O_2]$ will rise until the HF is consumed. Consider the recipe for $\langle 110 \rangle$ oriented nanowires (Table I Case c), shutting the HF source after reaching the steady-state etch orientation effectively pushes the nanowire angle to the right of Fig. 4(h) until $\langle 100 \rangle$ is reached and halts after depletion. This behavior is exemplified in Fig. 5(a), where the HF source is bypassed by a small flow of N_2 with a 2-min period. The change in etch direction forms a kink in the nanowire. In contrast to the liquid phase, the programmable nature of VP-MacEtch allows for arbitrary changes in etching conditions within a single process. This preserves the ability to control the

angle, length, and number of kinked segments by the carrier flow, oncycle duration, and etch duration, respectively.

However, when utilizing reactant depletion to form kinks, the length of the pulse period changes the kink profile dramatically, as shown in Fig. 5. Comparing the number of reactant pulses (on and off) with the number of kinked segments reveals a 1:1 correspondence of pulses to kinks for the 2-min pulse period [Fig. 5(a)], but the 60-and 30-s recipes lose 1 and 1.5 kinking periods, respectively. Because the reactant lines are closed when the recipe ends and a dedicated N_2 line is used to flush the chamber, the loss of kinking periods indicates that each pulse takes between 45 and 60 s to reach the sample. Furthermore, since the transit time is equal to or greater than the pulse period and the HF line is left open during the off-cycle, the next pulse has started before the previous pulse enters the chamber. This may cause the pulses to overlap, which prevents the etch from reaching the steady-state orientation and depletion (returning to $\langle 100 \rangle$).

3. Zigzag nanowires

If instead of bypassing the HF source the line is also toggled to vent, the change in orientation forms zigzag nanowires like in Figs. 6(a) and 6(b). Toggling HF to the vent line prevents overlapping pulses and flushes the remaining reactant from the line. Increasing the pulse duty cycle from 50% to 75% increases the amount of HF yielding a greater segment length. Notably, at the edge of the abruptly pulsed samples kinking occurs (Fig. S9) rather than zigzags (Fig. S9), which was also reported by Chen *et al.* for diffusion-controlled zigzag formation in the liquid phase. The enhanced diffusion around the sample's edge prefers kink formation, and as the pulse travels across the sample HF is consumed such that there are fewer kinking periods than reactant pulses.

To understand why altering the reactor's valve states changes the process from being depletion-driven (kinks) to diffusion-driven

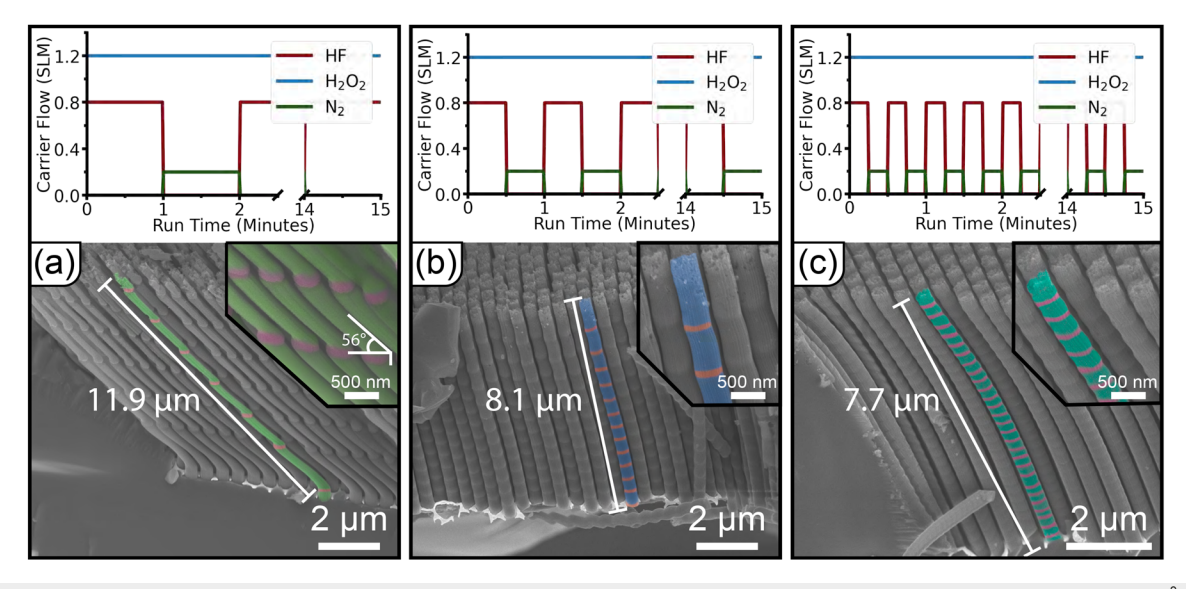


FIG. 5. Asynchronous pulse-mode VP-MacEtch on Si(100) with varying periods for 15 min at a 50% duty-cycle, with a H_2O_2 molar ratio of $\rho[H_2O_2] = 9.09 \times 10^{-2}$. (a) $\langle 110 \rangle$ -oriented nanowires with periodic kinking formed with a pulse period of 120 s. (b) Kinked nanowires processed with a pulse period of 60 s. (c) Kinked nanowires are processed with a pulse period of 30 s.

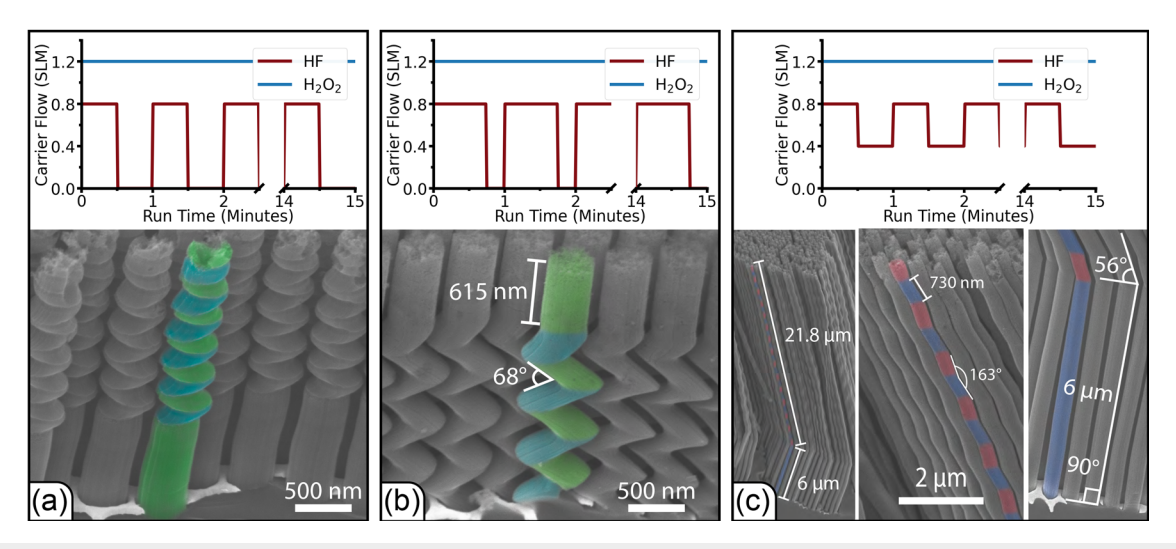


FIG. 6. False-color cross-sectional SEM images of periodically kinked nanowire arrays. All etches are 15 min in length on Si(100) substrates. (a) Kinked nanowires formed under continuous peroxide flow; the HF line is pulsed on at $\rho[H_2O_2]=9.09\times10^{-2}$ and switched to vent with a period of 1 min and a duty cycle of 50%. (b) Zigzag nanowires formed under an identical process as (a), but with a 75% duty cycle. (c) H_2O_2 molar-ratio modulated nanowires; the HF line is left open at $\rho[H_2O_2]=9.09\times10^{-2}$ and increased to 16.7×10^{-2} with a period of 1 min and a duty cycle of 50%.

(zigzags), the kinetics of mass transport between nanowires must be considered. Because the throttle valve is held in a fixed position for the course of the etch, abruptly cutting 40% of the total volumetric flow causes the chamber pressure to drop approximately 100 Torr. Assuming a pure N₂ atmosphere in the reactor, the mean free path $\lambda_{\rm mfp}$ may be approximated as 156 and 130 nm for 500 and 600 Torr, respectively [Eq. (S.1)]. Given the mean distance between nanowires is 100 nm, the ratio of $\lambda_{\rm mfp}$ to the width of the diffusion channel a, also called the Knudsen number, $Kn = \lambda_{\rm mfp}/a$ is 1.56 and 1.3 for 500 and 600 Torr, respectively. This places the transport kinetics into the transitional region between continuum and free molecular flow, also called Poiseuille flow where gas motion is driven by a pressure gradient This gradient $\Delta P_{channel}$ is usually considered much smaller than the bulk pressure, so $\Delta P_{channel} \ll P_R$; therefore, when the pressure drops by nearly 20% the pressure inside the channel is now greater than the reactor $P_{channel} > P_R$, so the diffusion direction will reverse. However, the mechanism by which the etch switches orientation is unclear as the reactants will diffuse at different rates based on their mass and overall concentration.

It was reported that in the liquid phase, zigzag formation only occurs after etching along the $\langle 100 \rangle$ direction for more than 1 μ m. ⁴⁶ At short lengths, the reaction cannot be driven to the diffusion-limited regime by suppressing the transport of H_2O_2 until a critical length is reached. The critical length is substantially smaller in the vapor phase at approximately 200 nm for a 50% duty cycle [Fig. 6(a)] and 615 nm for a 75% duty cycle [Fig. 6(b)]. The increased critical length for a 75% duty cycle is due to the initial on-cycle being longer. The overall reduction in critical length using this method is owed to the diffusion reversal occurring both in the boundary layer and shorter channels.

Abrupt pulsing, especially at periods near the pulse's transit time to the reactor, massively reduces the flux of HF by toggling to vent. This causes the aforementioned positional depletion, but also dramatically reduces the overall etch depth to only a few μ m. Because the etch orientation is also dependent on $\rho[H_2O_2]$, zigzags may also be formed

without sacrificing the etch rate by periodically reducing the flow of HF into the reactor as in Fig. 6(c). Under this scheme, the critical length practically vanishes, and the etch rate of 1.85 μm min $^{-1}$ exceeds that of both constituent recipes when run continuously (Fig. 4). The rate increase is likely owed to the periods of reduced HF flow, where the source can recover slightly. This is further supported by the increased length of the wire's angled portion compared to continuous operation, as upon HF depletion the etch returns to $\langle 100 \rangle$ (Fig. S4). Regardless of the pulsing scheme, the ability to controllably select and change the etch direction within a single process illustrates VP-MacEtch's power for 3D nanofabrication.

E. Ruthenium on silicon and VUV-enhanced VP-MacEtch

Ruthenium (Ru) is a promising catalyst for MacEtch at scale. Unlike the noble metals widely used in MacEtch (e.g., Au, Ag, Pt, and Pd), Ru is CMOS-compatible and is already used in semiconductor manufacturing processes as a diffusion barrier for interconnects.⁵⁷ Additionally, the international roadmap for devices and systems list Ru as the next interconnect metal for logic devices and DRAM capacitors. 58,59 Other CMOS-compatible MacEtch catalysts demonstrated include TiN, ¹⁶ graphene, ⁶⁰ and W. ⁶¹ However, the catalytic activity of these materials are much higher than the conventional noble metal MacEtch catalysts, which manifests as excess hole generation and a tendency to produce porosity in Si even at low aspect ratios. 62,63 A recent study by Mallavarapu et al. demonstrated treating the Ru catalyst with an argon plasma reduces the catalytic activity, enabling high-aspect ratio non-porous nanostructures.⁶³ However, the surface modifications alone are unable to achieve large area catalyst coverage, instead, requiring less than 50% coverage of the sample (patterning within circular areas with 250 μ m in diameter and 300 μ m spacing).

Although VP-MacEtch can eliminate the porous surface formation for Au on Si, this behavior is not extended to a Ru catalyst under forward-etching conditions (Fig. S10). Here, by decreasing the reactant flow and working pressure such that the MacEtch reaction occurs in the mass-transport limited regime, we demonstrate the first photo-enhanced $h\nu$ -MacEtch of Si under illumination. For this work, vacuum ultraviolet light (VUV) at a wavelength of $\lambda = 172 \text{ nm}$ was used. Figure 7 highlights the effect of VUV exposure on Si MacEtch. The catalyst pattern is a 5-nmthick Ru dot array with 4 μ m diameter and 4 μ m spacing. The etching condition is in the low pressure strongly mass-transport limited regime $(f[H_2O_2] = 50 \text{ sccm}, p_v[H_2O_2] = 1.3 \text{ Torr}, P_R =$ 225 Torr, and $\rho[H_2O_2] = 7.5 \times 10^{-3}$). Figure 7(a) shows the nonporous forward MacEtch by the Ru dots for 15 min in the absence of VUV, where the Ru metal catalyst is disintegrated presumably due to non-uniform etching-induced stress (Fig. S10), resulting in the rough morphology on the bottom surface which is also observed for thin catalyst films in the liquid phase.⁶⁴ Figure 7(b) displays the first demonstration of VUV-enhanced MacEtch for

15 min with an outer diameter at the top of 5.7 μ m and a depth of 2.8 μ m. The low working pressure used here limits the diffusion of reactants under the catalyst, slowing down the forward etching rate. In the meantime, the VUV excitation creates electron–hole pairs in exposed areas (all but the metal-covered area) enabling the MacEtch reaction in the region surrounding the catalyst, as in the liquid phase for GaN, ²⁵ SiC, ²⁷ and β -Ga₂O₃. ^{28,29} Note that $h\nu$ -MacEtch is inherently inverse, where etching starts from areas that are not covered by the catalyst. The simultaneous forward and inverse MacEtch process results in the formation of an array of uniform microwells with a smooth curved basin-like sidewall profile. Note that VUV alone does not etch Si in the absence of the metal catalyst (Fig. S11).

Because of the shallow penetration depth of 172 nm photons and hence the limited carrier generation rate, the VUV enhanced MacEtch rate depends on the distance to the metal catalyst for electron extraction, hence the upward sloping curvy sidewall profile centered around the catalyst. The microwell periphery continues to extend laterally as the bottom of the well sinks while the etching proceeds. Figure 7(c)

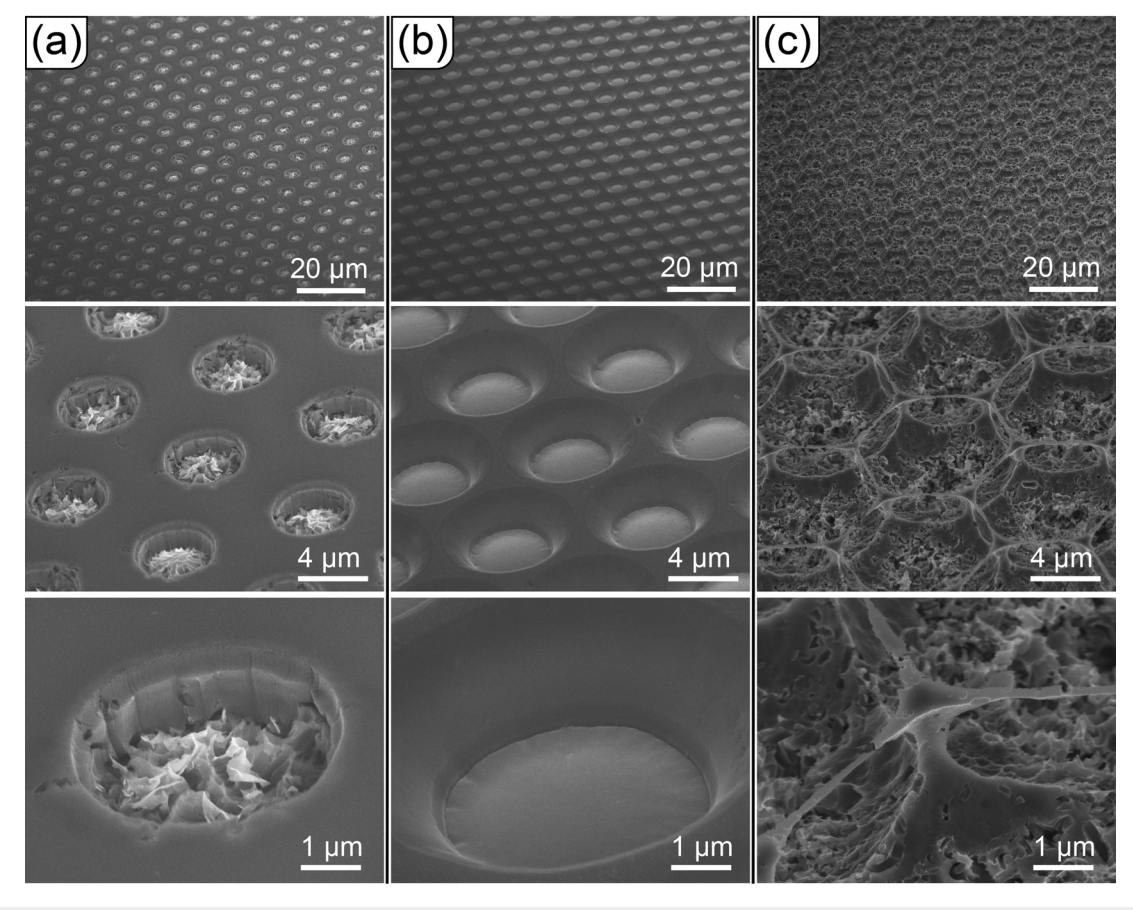


FIG. 7. VUV-assisted Etching of 5 nm thick Ruthenium dots on Si(100), with all samples etched at f[HF] = 250 sccm, $f[H_2O_2] = 50$ sccm, $P_R = 225$ Torr, $p_V[H_2O_2] = 1.3$ Torr, and $\rho[H_2O_2] = 7.5 \times 10^{-3}$. (a) Control sample etched without VUV for 15 min, the uneven sinking from the low working pressure causes catalyst failure. (b) Ruthenium micro-wells etched with VUV for 15 min, the excess carriers generated by $h\nu$ -MacEtch enable the oxidation and etching of the substrate surrounding the dots, while the forward-etch is not completely arrested. (c) VUV etching of Ru-dots for 30 min, as the etch continues the lateral etching regions connect to form a scaffold of nanowires across the top plane of the substrate (see also Fig. S12). Note the pattern failure occurs as the MgF₂ window is coated with residue from carbon tape (Fig. S13).

shows the etch profile after 30 min by VUV-enhanced MacEtch, where the curved etch profiles around the Ru dots intersect with its nearest neighbors, leaving behind a scaffold of interconnected nanowires at the Si surface. The rough morphology surrounding the hanging scaffold is a result of decreasing transmission of the VUV photons during the etch, which reverts the etch to the forward-etch mode of failure (details can be found in the supplementary material Fig. S13).

The demonstration of $h\nu$ -MacEtch in the vapor phase marks an important milestone in the unification and extension of the capabilities of liquid and vapor phase MacEtch. $h\nu$ -MacEtch plays a critical role in the MacEtch of wide-bandgap materials (GaN, SiC, and β -Ga₂O₃), enabling carrier generation in situations where the chemical potential of reactants or the intrinsic carrier mobility is insufficient to initiate the MacEtch reaction. Furthermore, the VUV light does not transmit in the ambient atmosphere or liquids due to the strong absorption of the high energy (7.2 eV) photons, which prevents its use in either liquid phase or thermal vapor MacEtch. By combining new etching chemistries and photon energies, photo-enhanced VP-MacEtch offers a highly promising avenue for MacEtch of previously demonstrated and new ultra-wide-bandgap semiconductors with more controllable etch rate and significantly improved scalability.

In summary, we have reported for the first time a fully programmable vapor-phase MacEtch process producing highly uniform and unique Si nanostructures that are otherwise difficult to form. Compared to bottom-up growth such as self-organized growth of nanowires, the cost of ownership of MacEtch is typically much lower. By independently controlling the influence of the etching precursors in the reaction, we have systematically presented various modes of precursor injection, including continuous and pulsed mode, synchronous and asynchronous pulsed mode, with pulse duration and period deterministically controlled. We have discussed the effect of precursor delivery, depletion and acceleration on MacEtch rate, MacEtched nanowire orientation. Versatile Si micro- and nanostructures, including nanowire arrays that are vertical, kinked, and zigzagged with arbitrary periods, as well as along various directions, have been produced, all without porosity and agglomeration. In addition, we have integrated a light source in the VP-MacEtch setup, allowing the additional degree of freedom of light exposure to MacEtch fabrication. For Si, VUV enhanced MacEtch takes place with simultaneous forward and inverse mechanisms but spatially separated, leading to smoothly curved microwell structures that have never been realized before.

This work represents a major milestone in the development of MacEtch nanotechnology by demonstrating independent control of the etchants in vapor phase. Several challenges VP-MacEtch has to be addressed in order to achieve full control of the programmability and uniformity. Two aspects of the technical challenges are the supply of reactants at the source and the delivery of reactants to the samples. The former challenge, the supply of reactants, limits both the maximum etch rate and the range of potential molar ratios, which may be addressed by alternate reaction chemistries with gaseous sources, the use of multiple sources in parallel, or higher capacity sources. The latter challenge, the delivery of reactants, limit the uniformity as the horizontal flow of reactants depletes across the sample. Just like other vapor phase processes, this may be resolved by switching to a vertical flow configuration at the cost of line-of-sight for VUV excitation. Despite these remaining challenges, the successful demonstration of MacEtch entirely and continuously in the vapor phase sets the foundation for translating this technique from lab to fab, and fully takes advantage of its simplicity, versatility, and scalability. In addition, there is no doubt that photo-enhanced VP-MacEtch will open up new possibilities in the 3D structures producible with MacEtch in the damage-free fashion, especially for wide and ultrawide bandgap semiconductors.

III. EXPERIMENTAL SECTION

The VP-MacEtch reactor, as illustrated in Fig. 1, consists of a reaction chamber, a gas manifold that programs the mass flow and valve state of each reaction precursor through a computer, and an exhaust system. The controller writes flow values to each of the two sets of mass flow controllers (MFC) for HF and H₂O₂, with one carrier MFC setting the flow through the bubbler and one dilution MFC adding additional carrier gas to the line. Note that the dilution MFC was set to zero for all the experiments reported here. There are two sets of primary valves; the bubbler bypass valve disconnects the source from the line and allows the same volumetric flow of nitrogen through the line, and the run/vent toggle valve disconnects the reactant line from the reactor and switches it to the vent line (directly to the vacuum pump). At the start of each experiment, the sources are bypassed and N₂ is flown into the system at the same rate as the experiment. During the N₂ purge the manual throttle valve is set, to fix the working pressure when the sources are switched on. Following the experiment, the sources are immediately switched to vent and a dedicated line is used to flush the reactor with N_2 .

Caution! Corrosive/Toxic HF liquid and vapor were only handled in small quantities in a fume hood. The entire experimental apparatus was contained within a fume hood. Neoprene gloves and liners, face shields, and standard lab PPE were worn when working on the system. The fume hood sash was always placed in its lowest position during experiments and maintenance.

The etchant bubbler source was a custom vessel filled with HF (50 wt. %), which is replaced between experiments such that the vapor pressure of $p_{\nu}[HF] = 30 \text{ Torr (Ref. 65)}$ remains constant. The oxidizer source was an anhydrous-H2O2 vessel purchased from RASIRC (San Diego, CA), of the constant vapor pressure of $p_v[H_2O_2] = 1.3$, or 2.1 Torr. Because the working pressure of the reactor is an order of magnitude greater than the reactant vapor pressures, it may be assumed that the pressure inside the bubblers is equal to that of the reactor and the sources and sample are at room temperature.⁴ Therefore, the volumetric flow of the reactant out of each source is dependent only on the carrier flow of reactant X(f[X]), vapor pressure $(p_{\nu}[X])$, and reactor pressure (P_R) as given by Eq. (5). 40 Under these assumptions, the analogous effective molar ratio flown into the reactor is presented in Eq. (6),

$$f_{out}[X] = \frac{f[X]p_{\nu}[X]}{P_R - p_{\nu}[X]},$$
 (5)

$$f_{out}[X] = \frac{f[X]p_{\nu}[X]}{P_{R} - p_{\nu}[X]},$$

$$\rho_{eff}[H_{2}O_{2}] = \frac{f_{out}[H_{2}O_{2}]}{f_{out}[HF] + f_{out}[H_{2}O_{2}]}.$$
(6)

All silicon wafers used in the experiment were p-type single-crystalline wafers [(100)-oriented, boron-doped, resistivity: 1–10 Ω cm] purchased from University Wafer (MA). Wafers were cleaned by a buffered oxide etch before patterning with either nanosphere

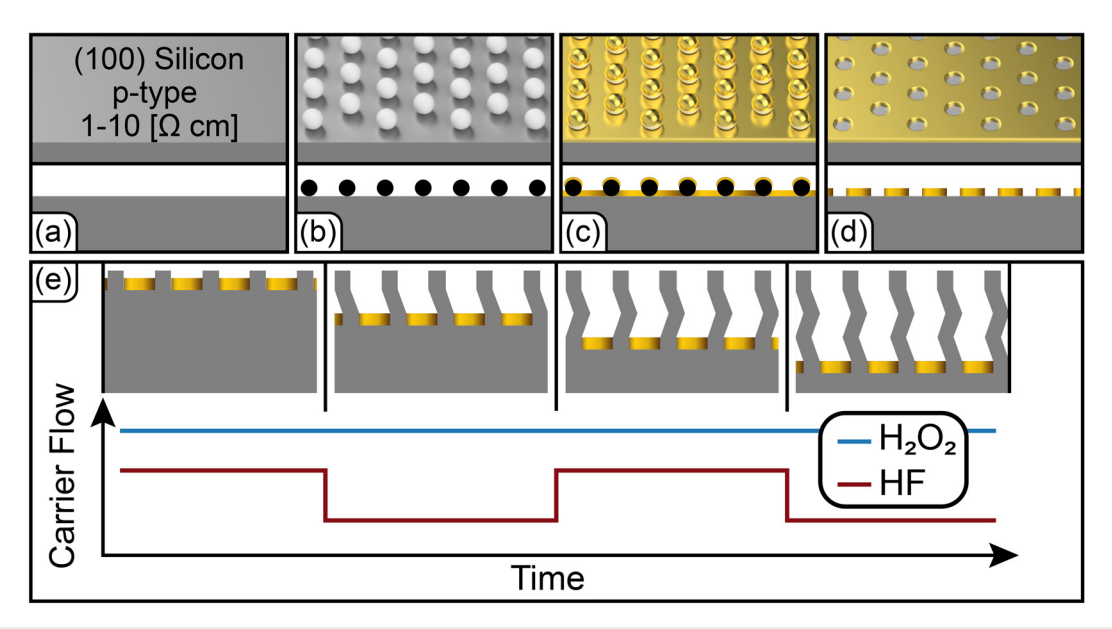


FIG. 8. Schematic diagram of VP-MacEtch nanowire process: (a) Bare p-type (100)-Si cleaned with a buffered oxide etch; (b) self-assembly and diameter reduction of polystyrene (PS) nanospheres; (c) metal deposition; (d) PS nanosphere liftoff; and (e) zigzag nanowire formation schematic; as the reactants enter the chamber and the molar ratio stabilizes the etch follows the (100) direction, as the ratio of the reactants is asymmetrically modulated, the etching direction alternates periodically.

lithography or photolithography. Figures 8(a)-8(d) illustrate the generalized nanosphere lithography process to produce a metal mesh pattern. Nanospheres with 500 nm diameter purchased from VWR were deposited with a modified Langmuir–Blodgett process. After sphere deposition, their diameters were reduced to 400 nm with an O_2 plasma step [Fig. 8(b)]. Following this, 60 nm of Au or 5 and 10 nm of Ru were deposited using a Lesker E-beam evaporator and AJA Orion sputtering system, respectively [Fig. 8(c)]. After liftoff, PDMS encapsulation for the nanospheres and acetone for the photoresist [Fig. 8(d)]. Before etching, all samples are degreased and have their oxide removed by another buffered oxide etch, and the patterned wafers are cleaved into approximately $2 \times 2 \, \text{cm}^2$ samples. Figure 8(e) illustrates the VP-MacEtch process with periodic modulation of the HF flow, while keeping the H_2O_2 flow constant, resulting in an array of zigzag nanowires. Details are presented in Sec. II.

In addition, photo-enhanced experiments were carried out with a 172 nm VUV lamp (11 mW/cm² at 172 nm) purchased from Cygnus Photonics. Etched structure morphology was characterized with an FEI scanning electron microscope (SEM) after cleaving the square silicon samples along their center axis (in the direction of the gas flow across the sample).

SUPPLEMENTARY MATERIAL

See the supplementary material for the discussion of nanowire fabrication, mass transport effects, reactant depletion, Ru forward MacEtch, and VUV-MacEtch.

ACKNOWLEDGMENTS

This work was supported in part by United States Army Research Office Award No. W911NF2110337, National Science Foundation ECCS No. 2200651, and a gift from Lam Research.

AUTHOR DECLARATIONS

Conflict of Interest

The authors have no conflicts to disclose.

Author Contributions

Lukas Leonard Janavicius: Conceptualization (equal); Investigation (lead); Writing – original draft (equal). Julian Michaels: Investigation (supporting); Writing – review & editing (supporting). Clarence Y. Chan: Investigation (supporting). Dane J. Sievers: Investigation (supporting). Xiuling Li: Funding acquisition (lead); Conceptualization (equal); Investigation (supporting); Writing – review & editing (equal).

DATA AVAILABILITY

The data that support the findings of this study are available from the corresponding author upon reasonable request.

REFERENCES

¹W. Kim, L. Güniat, A. Fontcuberta I Morral, and V. Piazza, Appl. Phys. Rev. 8(1), 011304 (2021).

²P. Wang, W. Lee, J. P. Corbett, W. H. Koll, N. M. Vu, D. A. Laleyan, Q. Wen, Y. Wu, A. Pandey, J. Gim, D. Wang, D. Y. Qiu, R. Hovden, M. Kira, J. T. Heron, J. A. Gupta, E. Kioupakis, Z. Mi, P. Wang, W. Lee, D. A. Laleyan, Q. Wen, Y. Wu, A. Pandey, D. Wang, M. Kira, Z. Mi, J. P. Corbett, W. H. Koll, J. A. Gupta, N. M. Vu, J. Gim, R. Hovden, J. T. Heron, E. Kioupakis, and D. Y. Qiu, Adv. Mater. 34(21), 2201387 (2022).

³X. Yuan, D. Pan, Y. Zhou, X. Zhang, K. Peng, B. Zhao, M. Deng, J. He, H. H. Tan, and C. Jagadish, Appl. Phys. Rev. 8(2), 021302 (2021).

⁴K. Ishikawa, K. Karahashi, T. Ishijima, S. I. Cho, S. Elliott, D. Hausmann, D. Mocuta, A. Wilson, and K. Kinoshita, Jpn. J. Appl. Phys., Part 1 57(6), 06JA01 (2018).

⁵S. W. D. Lim, M. L. Meretska, and F. Capasso, Nano Lett. **21**(20), 8642 (2021).

- ⁶H. Seong, S. G. Higgins, J. Penders, J. P. Armstrong, S. W. Crowder, A. C. Moore, J. E. Sero, M. Becce, and M. M. Stevens, ACS Nano 14(5), 5371 (2020).
 ⁷X. Li, Curr. Opin. Solid State Mater. Sci. 16(2), 71 (2012).
- ⁸Z. Huang, N. Geyer, P. Werner, J. de Boor, U. Gösele, Z. Huang, N. Geyer, P. Werner, J. de Boor, and U. Gösele, Adv. Mater. 23(2), 285 (2011).
- ⁹H. C. Huang, Z. Ren, C. Chan, and X. Li, J. Mater. Res. 36(23), 4756 (2021).
- ¹⁰W. McSweeney, H. Geaney, and C. O'Dwyer, Nano Res. 8(5), 1395 (2015).
- ¹¹M. Y. Arafat, M. A. Islam, A. W. B. Mahmood, F. Abdullah, M. Nur-E-Alam, T. S. Kiong, and N. Amin, Sustainability 13(19), 10766 (2021).
- ¹²L. Romano, M. Kagias, J. Vila-Comamala, K. Jefimovs, L. T. Tseng, V. A. Guzenko, and M. Stampanoni, Nanoscale Horiz. 5(5), 869 (2020).
- ¹³ K. Balasundaram, J. S. Sadhu, J. C. Shin, B. Azeredo, D. Chanda, M. Malik, K. Hsu, J. A. Rogers, P. Ferreira, S. Sinha, and X. Li, Nanotechnology 23(30), 305304 (2012).
- ¹⁴X. Li and P. W. Bonn, Appl. Phys. Lett. 77(16), 2572 (2000).
- ¹⁵K.-Q. Peng, Y.-J. Yan, S.-P. Gao, and J. Zhu, Adv. Mater. 14(16), 1164 (2002).
- ¹⁶J. D. Kim, M. Kim, C. Chan, N. Draeger, J. J. Coleman, and X. Li, ACS Appl. Mater. Interfaces 11(30), 27371 (2019).
- ¹⁷M. Kim, S. Yi, J. D. Kim, X. Yin, J. Li, J. Bong, D. Liu, S. C. Liu, A. Kvit, W. Zhou, X. Wang, Z. Yu, Z. Ma, and X. Li, ACS Nano 12(7), 6748 (2018).
- ¹⁸M. Dejarld, J. C. Shin, W. Chern, D. Chanda, K. Balasundaram, J. A. Rogers, and X. Li, Nano Lett. 11(12), 5259 (2011).
- ¹⁹L. Kong, Y. Song, J. D. Kim, L. Yu, D. Wasserman, W. K. Chim, S. Y. Chiam, and X. Li, ACS Nano 11(10), 10193 (2017).
- ²⁰P. Lova, V. Robbiano, F. Cacialli, D. Comoretto, and C. Soci, ACS Appl. Mater. Interfaces 10(39), 33434 (2018).
- ²¹T. S. Wilhelm, A. P. Kolberg, M. A. Baboli, A. Abrand, K. A. Bertness, and P. K. Mohseni, ECS J. Solid State Sci. Technol. 8(6), Q134 (2019).
- ²²S. H. Kim, P. K. Mohseni, Y. Song, T. Ishihara, and X. Li, Nano Lett. 15(1), 641 (2015).
- ²³Y. Song, P. K. Mohseni, S. H. Kim, J. C. Shin, T. Ishihara, I. Adesida, and X. Li, IEEE Electron Device Lett. 37(8), 970 (2016).
- ²⁴D. M. Dryden, R. J. Nikolic, and M. S. Islam, J. Electron. Mater. 48(5), 3345 (2019).
- ²⁵C. Y. Chan, S. Namiki, J. K. Hite, M. A. Mastro, S. B. Qadri, and X. Li, J. Vac. Sci. Technol. A 39(5), 053212 (2021).
- ²⁶Y. Liao, S. H. Shin, and M. Kim, Appl. Surf. Sci. 581, 152387 (2022).
- ²⁷J. A. Michaels, L. Janavicius, X. Wu, C. Chan, H. C. Huang, S. Namiki, M. Kim, D. Sievers, and X. Li, Adv. Funct. Mater. 31, 2103298 (2021).
- ²⁸M. Kim, H. C. Huang, J. D. Kim, K. D. Chabak, A. R. K. Kalapala, W. Zhou, and X. Li, Appl. Phys. Lett. 113(22), 222104 (2018).
- ²⁹H. C. Huang, M. Kim, X. Zhan, K. Chabak, J. D. Kim, A. Kvit, D. Liu, Z. Ma, J. M. Zuo, and X. Li, ACS Nano 13(8), 8784 (2019).
- ³⁰H. C. Huang, Z. Ren, A. F. Anhar Uddin Bhuiyan, Z. Feng, Z. Yang, X. Luo, A. Q. Huang, A. Green, K. Chabak, H. Zhao, and X. Li, Appl. Phys. Lett. 121(5), 052102 (2022).
- ³¹J. D. Kim, M. Kim, L. Kong, P. K. Mohseni, S. Ranganathan, J. Pachamuthu, W. K. Chim, S. Y. Chiam, J. J. Coleman, and X. Li, ACS Appl. Mater. Interfaces 10(10), 9116 (2018).
- ³²K. Rykaczewski, O. J. Hildreth, C. P. Wong, A. G. Fedorov, and J. H. J. Scott, Nano Lett. 11(6), 2369 (2011).
- ³³L. Romano, J. Vila-Comamala, K. Jefimovs, and M. Stampanoni, Microelectron. Eng. 177, 59 (2017).
- 34O. J. Hildreth and D. R. Schmidt, Adv. Funct. Mater. 24(24), 3827 (2014).
- 35M. D. Henry, C. Welch, and A. Scherer, J. Vac. Sci. Technol. A 27, 1211 (2009).
- 36V. T. H. Nguyen, F. Jensen, J. Hübner, P. Leussink, and H. Jansen, J. Vac. Sci. Technol. A 38(4), 043004 (2020).

- ³⁷F. J. Wendisch, M. Abazari, H. Mahdavi, M. Rey, N. Vogel, M. Musso, O. Diwald, and G. R. Bourret, ACS Appl. Mater. Interfaces 12(11), 13140 (2020).
- ³⁸ A. Mallavarapu, P. Ajay, and S. V. Sreenivasan, Nano Lett. **20**(11), 7896–7905 (2020).
- ³⁹O. J. Hildreth, W. Lin, and C. P. Wong, ACS Nano 3(12), 4033 (2009).
- ⁴⁰S. Berkman, V. S. Ban, and N. Goldsmith, *Heteroepitaxial Semiconductors for Electronic Devices* (Springer, New York, 1978), pp. 264–281.
- ⁴¹L. Kong, B. Dasgupta, Y. Ren, P. K. Mohseni, M. Hong, X. Li, W. K. Chim, and S. Y. Chiam, Sci. Rep. 6(1), 36582 (2016).
- ⁴²W. Chern, K. Hsu, I. S. Chun, B. P. Azeredo, N. Ahmed, K. H. Kim, J. M. Zuo, N. Fang, P. Ferreira, and X. Li, Nano Lett. 10(5), 1582 (2010).
- ⁴³F. J. Wendisch, M. Rey, N. Vogel, and G. R. Bourret, Chem. Mater. 32(21), 9425 (2020).
- 44 S. K. Song, H. Saare, and G. N. Parsons, Chem. Mater. 31(13), 4793 (2019).
- ⁴⁵J. Hennessy, C. Moore, K. Balasubramanian, A. Jewell, C. Carter, K. France, and S. Nikzad, Proc. SPIE 10401, 1040119 (2017).
- 46Y. Chen, C. Zhang, L. Li, C. C. Tuan, F. Wu, X. Chen, J. Gao, Y. Ding, and C. P. Wong, Nano Lett. 17(7), 4304 (2017).
- ⁴⁷B. A. Sperling and J. E. Maslar, J. Vac. Sci. Technol. B **37**(6), 060907 (2019).
- ⁴⁸C. Y. Chen, C. S. Wu, C. J. Chou, and T. J. Yen, Adv. Mater. **20**(20), 3811 (2008).
- 49Y. Kim, A. Tsao, D. H. Lee, and R. Maboudian, J. Mater. Chem. C 1(2), 220 (2012).
- 50]. Kim, H. Han, Y. H. Kim, S. H. Choi, J. C. Kim, and W. Lee, ACS Nano 5(4), 3222 (2011).
- ⁵¹C. Y. Chen and C. P. Wong, Nanoscale 7(3), 1216 (2014).
- ⁵²H. Seidel, L. Csepregi, A. Heuberger, and H. Baumgärtel, J. Electrochem. Soc. 137(11), 3612 (1990).
- 53 Y. Chen, L. Li, C. Zhang, C. C. Tuan, X. Chen, J. Gao, and C. P. Wong, Nano Lett. 17(2), 1014 (2017).
- ⁵⁴H. Chen, H. Wang, X. H. Zhang, C. S. Lee, and S. T. Lee, Nano Lett. **10**(3), 864 (2010).
- 55A. Taassob, A. Bordbar, S. Kheirandish, and F. Sharipov, J. Micromech. Microeng. 9(4), 394 (1999).
- ⁵⁶F. Sharipov, Encyclopedia of Microfluidics and Nanofluidics (Springer, Boston, 2008), pp. 772–778.
- ⁵⁷T. N. Arunagiri, Y. Zhang, O. Chyan, M. El-Bouanani, M. J. Kim, K. H. Chen, C. T. Wu, and L. C. Chen, Appl. Phys. Lett. 86(8), 083104 (2005).
- ⁵⁸L. G. Wen, C. Adelmann, O. V. Pedreira, S. Dutta, M. Popovici, B. Briggs, N. Heylen, K. Vanstreels, C. J. Wilson, S. Van Elshocht, K. Croes, J. Bommels, and Z. Tokei, in *Proceedings of the IEEE International Interconnect Technology Conference/Advanced Metallization Conference* (IEEE, 2016), pp. 34–36.
- pp. 34–36.

 59 S. Paolillo, D. Wan, F. Lazzarino, N. Rassoul, D. Piumi, and Z. Tőkei, J. Vac. Sci. Technol. B 36(3), 03E103 (2018).
- ⁶⁰J. Kim, D. H. Lee, J. H. Kim, and S. H. Choi, ACS Appl. Mater. Interfaces 7(43), 24242 (2015).
- ⁶¹O. Hildreth, C. Alvarez, and C. P. Wong, in *Proceedings of the Electronic Components and Technology Conference* (IEEE, 2010), pp. 794–797.
- 62D. Sadakane, K. Yamakawa, N. Fukumuro, and S. Yae, ECS Trans. 69(2), 179 (2015).
- ⁶³A. Mallavarapu, P. Ajay, C. Barrera, and S. V. Sreenivasan, ACS Appl. Mater. Interfaces 13(1), 1169 (2021).
- ⁶⁴Z. Huang, T. Shimizu, S. Senz, Z. Zhang, X. Zhang, W. Lee, N. Geyer, and U. Gösele, Nano Lett. 9(7), 2519 (2009).
- ⁶⁵N. Miki, M. Maeno, K. Maruhashi, and T. Ohmi, J. Electrochem. Soc. 137(3), 787 (1990).